Journal of the Ceramic Society of Japan 134 [4] 316-324 2026
DOI https://doi.org/10.2109/jcersj2.25158

JCS-Japan

FULL PAPER

Accelerating electrochemical CO_2-to-CO conversion with Zn–Al layered double hydroxide amorphized by grinding treatment

Ryosuke Nakazato[1,†], **Keeko Matsumoto**[2], **Matthias Quintelier**[3], **Joke Hadermann**[3], **Margherita Cavallo**[4], **Valentina Crocellà**[4], **Francesca Bonino**[4], **Nataly Carolina Rosero-Navarro**[2,5], **Yuta Fujii**[2], **Akira Miura**[2] and **Kiyoharu Tadanaga**[2,‡]

[1] National Institute of Advanced Industrial Science and Technology (AIST), Energy Process Research Institute,
16–1 Onogawa, Tsukuba, Ibaraki 305–8569, Japan
[2] Faculty of Engineering, Hokkaido University, Kita 13, Nishi 8, Kita-ku, Sapporo 060–8628, Japan
[3] EMAT, Department of Physics, University of Antwerp, Groenenborgerlaan 171, 2020 Antwerp, Belgium
[4] Dipartimento di Chimica, Centro NIS, Unità di Ricerca INSTM, Università di Torino,
Via G. Quarello 15/A and Via P. Giuria 7, I-10125 Torino, Italy
[5] Instituto de Cerámica y Vidrio, CSIC, C/Kelsen 5. Campus de Cantoblanco. 28049 Madrid, Spain

Carbon dioxide (CO_2) electrolysis is one of the promising technologies to convert CO_2 into value-added chemical compounds and has attracted attention in recent years from the perspective of energy crisis and carbon neutrality. For efficient CO_2 electrolysis, numerous attempts have been made to develop superior electrocatalysts that accelerate the CO_2 reduction reaction (CO_2RR), and their performance has been enhanced by controlling structure, morphology, and elemental composition. However, the effect of grinding treatment of catalysts on their structure, morphology, and CO_2RR activity is frequently underestimated, which is performed for grain refining of catalyst particles to achieve optimum activity in general. In the present paper, we focused on Zn–Al layered double hydroxide (LDH) as an electrocatalyst which has CO_2RR activity for carbon monoxide (CO) evolution. Zn–Al LDH and its ground samples for 10, 20, 30, and 60 min (Gx-LDHs, $x = 0$, 10, 20, 30, and 60, respectively) were prepared using a facile co-precipitation method and simple grinding with a mortar and pestle. Remarkably, Gx-LDHs exhibited superior activity for CO_2-to-CO conversion as grinding proceeded. In particular, the growth rate in partial current density of CO was 3.2-fold and 1.6-fold from G0-LDH (as-prepared) to G10-LDH and from G10-LDH to G60-LDH, respectively. XRD and TEM analysis showed that the crystal structure of Zn–Al LDH collapsed due to amorphization as grinding proceeded. XAFS analysis indicated that Zn sites in the amorphous phase are mainly in the low-valent Zn state ($Zn^{\delta+}$, $0 < \delta < 2$), which is a favorable state for CO_2-to-CO conversion. Our results highlighted that grinding treatment clearly affected the structural and morphological properties of Zn–Al LDH, enhancing its CO_2RR activity.

Key-words : CO_2 electrolysis, CO_2 reduction reaction (CO_2RR), CO evolution, Layered double hydroxide (LDH), Grinding treatment, Low-valent Zn, X-ray absorption fine structure (XAFS)

[Received November 20, 2025; Accepted January 9, 2026]

1. Introduction

Carbon dioxide (CO_2) electrolysis is a promising technology for converting CO_2 into value-added chemical compounds and has attracted attention from the perspective of carbon neutrality and the energy crisis.[1–6] Since CO_2 is an anthropogenic greenhouse gas driving global warming, and its atmospheric concentrations have increased from approximately 278 ppm at pre-industrial levels (before 1750) to 426 ppm in 2025,[7,8] global energy crisis, global warming, and environmental degradation caused by increasing CO_2 emissions are pressing issues. Highly active electrocatalysts enable the CO_2 reduction reaction (CO2RR) to be performed with high production rates and energy conversion efficiency, resulting in efficient CO_2 electrolysis, which is demanded for practical applications using electricity from renewable sources, such as solar and wind power.[9] Moreover, CO_2RR can serve various CO_2-conversion products [carbon monoxide (CO), methane, methanol, formic acid, and C_{2+} products], depending on the type of catalyst. Especially, CO is an important feedstock chemical for synthesizing methanol and liquid fuels,[10] and is known to be generated effectively by Au-,[11,12] Ag-,[13] and Zn-based catalysts. Non-noble metal-based catalysts, such as Zn, are desired from a practical

---

[†] Corresponding author: R. Nakazato; E-mail: nakazato-ryosuke@aist.go.jp

[‡] Corresponding author: K. Tadanaga; E-mail: tadanaga@eng.hokudai.ac.jp

©2026 The Ceramic Society of Japan

This is an Open Access article distributed under the terms of the Creative Commons Attribution License (https://creativecommons.org/licenses/by/4.0/), which permits unrestricted use, distribution, and reproduction in any medium, provided the original work is properly cited.

point of view but have not yet outperformed Au- and Ag-based ones in terms of selectivity and efficiency, which remains a significant challenge.[14] Various Zn-based compounds have been reported as excellent catalysts for CO_2-to-CO conversion, such as oxide,[15–19] non-oxide,[20–22] and single-atom catalysts (SAC).[23–26] Furthermore, their catalytic performance has also been improved by controlling structure and morphology as well as elemental composition. Meanwhile, grinding treatment is also used in general for grain refining of catalyst particles to achieve optimum activity, although it may affect the structure and morphology of a catalyst. However, the effect of grinding treatment is frequently underestimated. To the best of our knowledge, there are no reports in this field that clearly mention whether the catalyst is fragile or not, and what effects appear by grinding treatment.

To investigate the effect of grinding treatment on the structure, morphology, and CO_2RR activity of the catalyst, we focused on layered double hydroxides (LDH), which are known to be a fragile compound for grinding treatment. LDH has the chemical composition of $[M^{2+}{}_{1-x}M'^{3+}{}_{x}(OH)_2]^{x+}$ $[A^{n-}{}_{x/n}]^{x-}$, consisting of positively charged metal hydroxide layers ($[M^{2+}{}_{1-x}M'^{3+}{}_{x}(OH)_2]^{x+}$) and charge-compensating anions (A^{n-}) inserted between the layers. The presence of at least two metal ions characterizes LDH, represented by M^{2+}-M'^{3+} LDH. For the fragility of LDH, it has been reported that grinding treatment significantly altered the structural and morphological properties of well-crystallized Mg–Al LDH, resulting in the amorphous material without its pristine crystalline structure.[27] Despite its fragility, LDH has been studied for a long time as electrocatalysts for oxygen evolution (OER),[28–31] oxygen reduction reactions (ORR),[29,32,33] and hydrogen evolution reaction (HER),[31,34] due to their superior properties, such as diversity of metal compositions,[35] large specific surface area,[35] high hydroxide ion conductivity,[36,37] and high alkaline tolerance.[29–31,33] LDH has begun to be focused on as a CO_2RR catalyst in recent years.[38–47] We have reported that Zn-based LDHs, such as Zn–Al, Zn–Cr, and Zn–Ga LDHs, exhibited CO_2RR activity for CO evolution (i.e., $CO_2 + H_2O + 2e^- \rightarrow CO + 2OH^-$).[43–46] Other research groups reported that the CO selectivity of Zn–Al LDHs can be enhanced by the introduction of third metal species such as Mg^{2+} and Ce^{3+},[41,42] resulting in nearly 90 % Faraday efficiency of CO evolution (FE_{CO}). Furthermore, Cu-based LDHs have been reported to afford various CO_2-conversion products, such as methanol,[38] and formic acid,[39] acetic acid,[40] indicating a great potential of LDH as a CO_2RR catalyst.

Although LDH is a relatively fragile compound as mentioned above, most research on LDH-based CO_2RR catalysts did not describe a comparison of characterization before and after grinding treatment, and some studies did not provide detailed grinding conditions, such as the type of grinding method and duration time.[41,42] Such a situation is not limited to the research on LDH-based CO_2RR catalysts. We emphasize that grinding treatment is an important process that is often underestimated in the field of CO_2 electrolysis. In the present paper, we prepared Zn–Al LDH and its ground samples for 10, 20, 30, and 60 min (Gx-LDHs, $x = 0$, 10, 20, 30, and 60, respectively) using a previously reported co-precipitation method[17] and simple grinding with a mortar and pestle. As a result, the effect of grinding treatment for Zn–Al LDH was revealed to affect its structural and morphological properties, enhancing its CO_2RR activity.

2. Experimental

2.1 Materials

Zinc nitrate hexahydrate [$Zn(NO_3)_2 \cdot 6H_2O$, 99.0 %], aluminum nitrate nonahydrate [$Al(NO_3)_3 \cdot 9H_2O$, 98.0 %], sodium carbonate (Na_2CO_3, 99.8 %), potassium bicarbonate ($KHCO_3$, >99.5 %), and sodium hydroxide (NaOH, 97.0 %) were purchased from FUJIFILM WAKO PURE CHEMICAL Co. Water (H_2O) was purified by a distilled water production system (SHIMIZU SCIENTIFIC INSTRUMENTS MFG Co., Ltd.). An anion exchange membrane (AHA) was purchased from ASTOM Corp. CO_2 gas (>99.5 %) was purchased from TAIYO NIPPON SANSO HOKKAIDO Corp. All other solvents and chemicals in reagent grade were purchased and used without further purification.

2.2 Synthesis, grinding, and humidification of LDH samples

Zn–Al LDH (Zn/Al = 2:1) was synthesized using a facile and traditional co-precipitation process according to a literature procedure method,[45] and the as-prepared LDH was labeled G0-LDH. 160 mg of the G0-LDH was manually ground in a mortar (inside diameter 85 mm), and then 20 mg of the ground sample was collected every 10 min and labeled Gx-LDHs ($x = 10$, 20, 30). The remaining sample (100 mg) was further ground for 30 min and was labeled G60-LDH. Portions of the as-prepared LDH and the ground LDHs were humidified for 3 h at 25 °C and 90 % relative humidity in a constant temperature and humidity chamber (IW-221, YAMATO SCIENTIFIC Co., Ltd.), which were labeled Hx-LDH ($x = 0$, 10, 20, 30, 60). The product was characterized by X-ray diffraction (XRD), transmission electron microscopy (TEM), X-ray absorption fine structure (XAFS), Brunauer–Emmett–Teller (BET) analysis, and attenuated total reflectance infrared spectroscopy (ATR-IR). XRD patterns (Cu Kα) were obtained using an XRD diffractometer (Mini Flex 600, Rigaku Corp.) to identify the crystalline phase. The sample morphology was evaluated by TEM (Thermo Fisher Titan microscope, operated at 300 kV, image corrected and equipped with a Gatan K2 direct electron detector). The XAFS spectra were obtained at the BL5S1 of Aichi Synchrotron Radiation Center, Aichi Science & Technology Foundation, Aichi, Japan. XAFS measurements at the Zn-K edge were recorded in a transmission mode. Zn foil, ZnO, $Zn(OH)_2$, and $ZnCO_3$ were used as references. The obtained Fourier-transformed extended X-ray absorption fine structure (FT-EXAFS) data were processed according to the standard procedures using the ATHENA-ARTEMIS module implemented in the Demeter software packages. The specific surface area (SSA) of the samples was evaluated from the BET equation by measuring the adsorption isotherms of N_2 at 77 K with an automatic adsorption apparatus (BELSORP MINI II, MicrotracBEL Corp.) Before the measurements, the samples were degassed for 2 h at 120 °C to remove physically adsorbed H_2O molecules. The range of relative pressure (P/P_0) used for BET calculation was 0.01–0.3. ATR-IR measurements were performed using a Bruker Invenio Fourier transform spectrometer, equipped with a mercury cadmium telluride cryo-detector operated at liquid nitrogen temperature (~77 K), and a commercial horizontal ATR mirror unit and cell (HATR, Horizontal ATR accessory provided by Pike Technologies) equipped with an AMTIR single crystal (internal reflection element 80 × 10 × 4 mm, 45°, Specac). Each collected spectrum consists of an average of 32 scans (64 for the background spectrum). LDH samples, firstly suspended in ethanol (15 mg per 0.5 mL of ethanol), were deposited on the crystal and dried overnight. The sample was then flushed with liquid H_2O or C_6H_{12} saturated with N_2 or CO_2, which were supplied through a mass flow controller with a flow rate of 15 mL min^{-1}. Firstly, N_2-saturated H_2O or C_6H_{12} was circulated over the deposited LDH at room temperature for 30 min to verify the stability of the sample deposition. After that, the inlet gas was switched to CO_2 following the procedure reported in previous works.[44,45]

2.3 Preparation of the catalyst-loaded cathode

The catalyst-loaded cathode was prepared by simply drop-casting the catalyst ink on carbon paper (Sigracet 36BB, SGL CARBON JAPAN Ltd.). The catalyst ink was prepared by mixing 4 mg of the catalyst sample with 1 mg of the conductive aid (carbon black: Vulcan XC72, CABOT Corp.) and 30 µL of the binder (an anion exchange resin solution, TOKUYAMA Corp.) in 570 µL of ethanol and sonicating for 10 min. The catalyst ink was drop-casted onto carbon paper on a hot plate pre-heated at 80 °C. The ink coating area was 1.89 cm^2, whose shape was a 1.55 cm diameter circle, and the loading level of the LDH was 2.1 mg cm^{-2}. The catalyst-loaded cathode was dried at 80 °C for at least 30 min to remove the solvents.

2.4 CO_2 electrolysis experiment

CO_2RR with the catalyst-loaded cathode was performed in a three-compartment cell using a three-electrode setup[45] and a 1.0 M $KHCO_3$ aqueous solution as electrolyte. The cathodic and anodic compartments were separated by a piece of the anion exchange membrane to prevent the unexpected influence of the oxidation reaction taking place on the counter electrode. The LDH-loaded cathode and a platinum mesh anode (35 × 25 mm, LAKE SHORE CRVOTRONICS Inc.) were used as working and counter electrodes, respectively. An Ag/AgCl (3.0 M KCl, BAS Inc.) electrode was used as a reference. A pH meter (pH 700, EUTECH INSTRUMENTS Pte. Ltd.) was used to measure the pH of electrolytes. The CO_2 gas flowed with a 50 mL min^{-1} flow rate and 0.10 MPa inlet pressure to the cathodic compartment, while the solution in the reference electrode compartment was stirred at 600 rpm with a PTFE stirring bar. CO_2 electrolysis was performed with an electrochemical analyzer (IviumStat, IVIUM TECHNOLOGIES B.V.) under potentiostatic conditions for 10 min for each applied potential. Gaseous products were detected and quantified by gas chromatography techniques (GC-2014, SHIMADZU Corp.; carrier gas: nitrogen, flow rate: 10 ml min^{-1}, pressure: 53.2 kPa, vaporization chamber temperature: 120 °C). For the detection of hydrogen (H_2), Molecular Sieve 5A (GL SCIENCES Inc.; column temperature: 50 °C, injected sample volume: 1 mL) and a thermal conductivity detector (TCD, SHIMADZU Corp.; detector temperature: 120 °C) were used. For the detection of CO and gaseous hydrocarbons, PoraPak N (GL SCIENCES Inc.; column temperature: 50 °C, injected sample volume: 1 mL) for a flame ionization detector (FID, SHIMADZU Corp.; detector temperature: 120 °C) were used.

Electrode potentials in the study were converted to the reversible hydrogen electrode (RHE) or the standard hydrogen electrode (SHE) according to the following equations: $E_{RHE} = E_{SHE} + 0.059 \times \text{pH}$, $E_{SHE} = E_{Ag/AgCl} + 0.222\,\text{V}$. All potentials and voltages in this work were evaluated without *iR* calibration. The Faradaic efficiency (*FE*) for CO and H_2 was calculated based on the equations:

$$FE = \frac{i}{I}, \quad i = \frac{2VprF}{RT}$$

(= partial current of CO and H_2)

Where V was the volume concentration of CO or H_2 in the produced gas determined by GC-TCD. r was the CO_2 flow rate (m^3 s^{-1}) at ambient temperature and pressure, and I was the average current (A) during the reaction. For the other constants, p was 1.013×10^5 Pa, F was 96485 C mol^{-1}, R was 8.3145 J mol^{-1} K^{-1}, and T was 298 K.

3. Results and discussion

3.1 Structural and morphological characterization of the as-prepared and ground Zn–Al LDHs

The XRD patterns of the as-prepared product (G0-LDH) and its ground samples (Gx-LDHs, x = 10, 20, 30, and 60) are shown in **Fig. 1**. G0-LDH exhibited the peaks characteristic of Zn–Al LDH with CO_3^{2-} anions.[48] The sharp peaks and no other crystalline peaks indicate the high crystallinity and purity of the as-prepared product.

On the other hand, the intensity of all peaks decreased gradually in G10-, G20-, and G30-LDHs as grinding proceeded, indicating that the crystallinity of Zn–Al LDH decreased during the grinding treatment. After further grinding, the peaks derived from the LDH structure almost disappeared, as shown in the XRD patterns of G60-LDH.

Focusing on the pattern change in more detail, it should be noted that the (003) and (110) diffraction peaks were indicative of the periodicity of the Zn–Al LDH structure perpendicular and parallel to the layer, respectively. Figure S1 shows that the intensity of (003) diffraction peak decreased more predominantly than that of the non-(00l) diffraction peaks, meaning that the collapse of the crystal structure was more pronounced in the direction perpendicular to the layer than parallel to it. Therefore, delamination between the layers is considered to be a trigger of the collapse of the crystal structure. This interpretation is analogous to the previous study focusing on the milled Mg–Al LDH, which was indicated to form turbostratic structural disorder while retaining the two-dimensional layered structure in the initial grinding stage.[27)]

From the TEM images (**Figs. 2** and S2), the typical hexagonal and platelet-like morphologies were seen in the G0-LDH, as shown in Figs. 2(a) and 2(b). The particle size ranged from 100 to 500 nm in hexagonal orientation. The thickness of these particles varied from 9 to 35 nm. Figure 2(c) shows that G10-LDH also had some platelet-like particles, but most of the particles were very thin without a distinguishable morphology. The particle sizes ranged from 50 to 350 nm, which clustered together and often lacked distinctive edges between them. However, BET analysis showed no significant changes in SSA, as shown in Figs. S3(a) and S3(b). On the contrary, platelet-like particles and apparent morphology were not observed for G20-, G30-, and G60-LDHs [Figs. 2(d), 2(e), 2(f)], and their particle sizes were 40–150, 40–400, and 50–500 nm, respectively. This increase in particle size was supported by BET analysis, exhibiting a decrease in SSA as grinding proceeded. As shown in Figs. S3(a) and S3(c), the SSA of G60-LDH was 67 % less than that of G0-LDH.

High-resolution TEM (HRTEM) images obtained from platelet particles in G0-LDH were shown in Fig. S2(a), where atomic fringes with sizes ranging from 90 to 300 nm were observed, representing the metal hydroxide layers. G10-LDH was also observed to have fringes like them, whose sizes ranged from 10 to 90 nm, but those were sparser than in G0-LDH as shown in Fig. S2(b). As grinding proceeded, the fringes were gradually sparser and shortened, whose sizes were 10–30, 7, and 5 nm in G20-, G30-, and G60-LDHs [Figs. S2(c), S2(d), S2(e)], respectively. These results exhibited that some amorphous phases with no fringes occurred even from the initial grinding

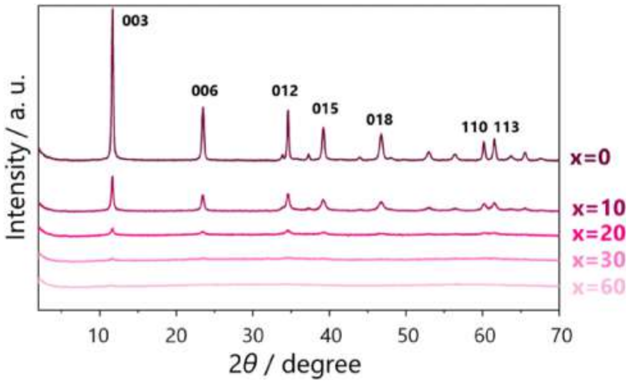

Fig. 1. XRD patterns of the as-prepared Zn–Al LDH (G0-LDH) and its ground samples for x min (Gx-LDH, $x = 10, 20, 30,$ and 60).

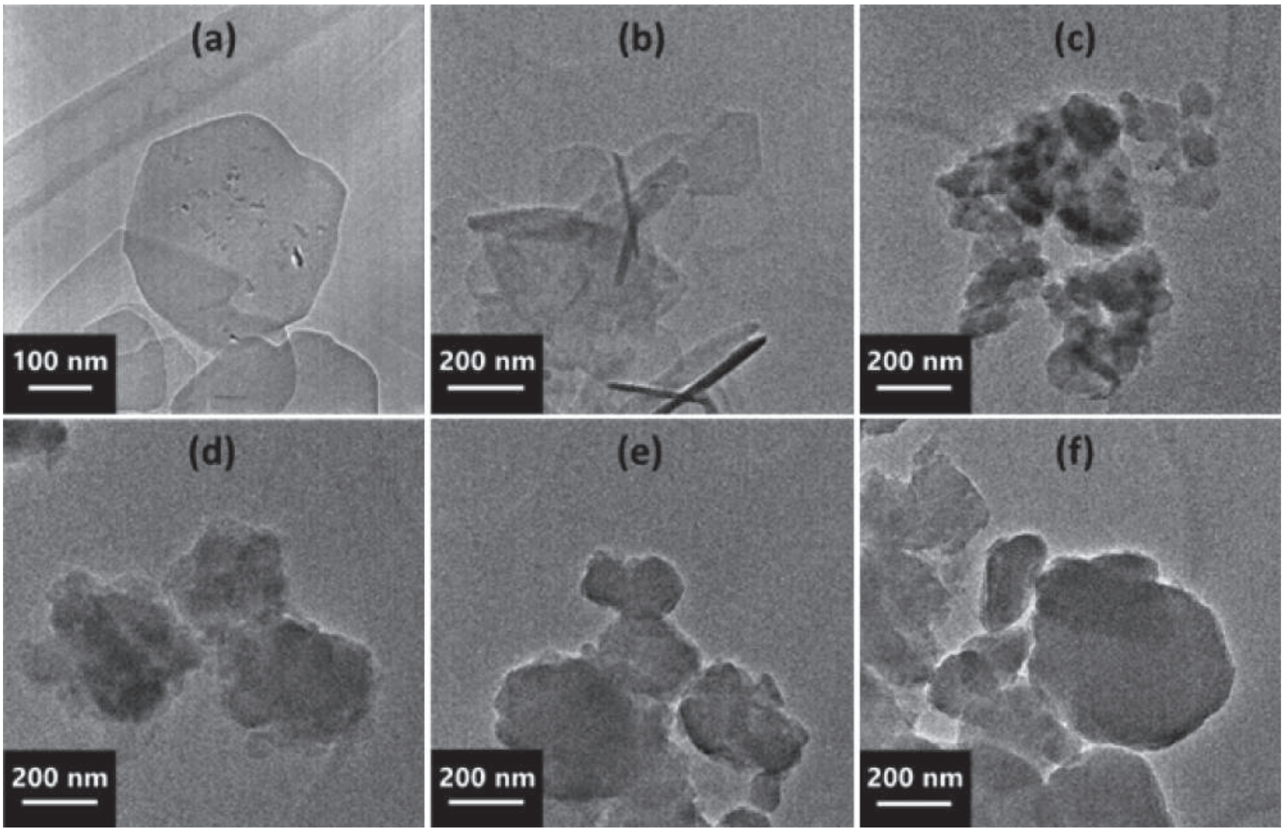

Fig. 2. TEM images of Gx-LDHs [(a, b) $x = 0$, (c) $x = 10$, (d) $x = 20$, (e) $x = 30$, (f) $x = 60$].

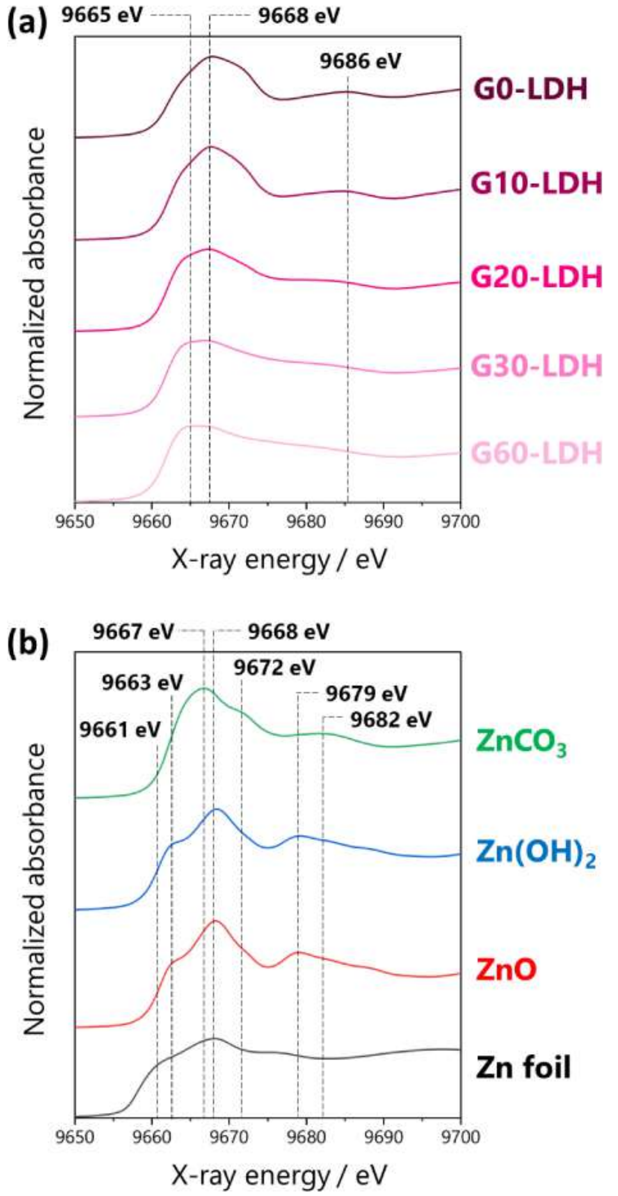

Fig. 3. Zn-K edge XANES spectra of (a) G*x*-LDHs ($x = 0$, 10, 20, 30, and 60) and (b) references [$ZnCO_3$, $Zn(OH)_2$, ZnO, and Zn foil].

stage, such as G10-LDH, and amorphization became more pronounced as grinding proceeded, resulting in the dominant amorphous phase at the final grinding stage, such as in G60-LDH.

The coordination environment and valence state of the Zn atoms were evaluated by XAFS analyses. The Zn-K edge X-ray absorption near edge structure (XANES) spectra for G*x*-LDH ($x = 0$, 10, 20, 30 and 60) and references [$ZnCO_3$, $Zn(OH)_2$, ZnO and Zn foil] are shown in **Fig. 3**. Zn–Al LDH exhibited a characteristic spectral shape with a peak top at 9668 eV in the non-ground state (G0-LDH),[49] which was different from all reference spectra, and gradually changes to a spectral shape with a peak top at 9665 eV (G60-LDH) as grinding proceeded. Considering the XRD and TEM results, the amorphous phase formed by grinding could correspond to the component with a peak top at 9665 eV, which is lower energy than the peak tops of the other Zn^{2+} compounds. For this reason, the Zn sites in the amorphous phase are considered to be mainly in a more reductive state than the divalent state (Zn^{2+}), implying the low-valent state ($Zn^{\delta+}$, $0 < \delta < 2$), which is not the metallic state (Zn^0) but more favorable state for CO_2RR to promote the adsorption and activation of CO_2.[21–23,50–52]

This hypothesis is supported by the FT-EXAFS spectra. Figure S4 exhibits clear peaks at 1.5 Å attributed to the Zn–O bond for all G*x*-LDHs and no peak at 2.3 Å corresponding to metallic Zn (Zn–Zn bond). Furthermore, peaks corresponding to Zn–O–Zn bonds appeared at 2.8–2.9 Å for references [$ZnCO_3$, $Zn(OH)_2$, and ZnO], while a characteristic peak corresponding to Zn–O–M (M: Zn or Al) bonds was observed at 2.7 Å for G10-LDH. This peak gradually decreased as grinding proceeded and almost disappeared in G60-LDH. Interestingly, the changes in the XANES and EXAFS spectral shape of Zn–Al LDH upon grinding are similar to those corresponding to the nanoparticulation of ZnO from 25 µm to 4.5 nm in particle size,[53] indicating that the Zn sites of amorphized Zn–Al LDH locate a similar coordination environment to ZnO nanoparticle, which has many grain boundaries with structural distortion and disorder. In such a disordered environment, Zn sites are coordinatively unsaturated, and thus $Zn^{\delta+}$ states are stabilized.[23] Taking together, XANES and EXAFS spectra consistently indicate that the Zn sites in amorphized Zn–Al LDH are mainly in $Zn^{\delta+}$ state.

3.2 The structural memory effect on the ground Zn–Al LDHs

The structural memory effect is a well-known property by which the layered structure of LDHs lost due to calcination at a certain temperature (300–500 °C) can be reconstructed by contact with H_2O.[31,54,55] This effect may also occur on ground LDHs (G*x*-LDHs) and affect its CO_2RR activity since CO_2 electrolysis is performed under conditions where the catalyst contacts with H_2O. Accordingly, we investigated the change in structure and morphology of humidified G*x*-LDHs (H*x*-LDHs). As a result, the TEM image of H60-LDH clearly showed that the lost hexagonal and platelet-like morphologies were regenerated by contact with H_2O as shown in Fig. S5, and Fig. S6 showed XRD patterns derived from the crystalline structure of LDH for all H*x*-LDHs ($x = 0$, 10, 20, 30, and 60), exhibiting that a memory effect occurs for ground LDHs. Notably, the samples ground for a longer time showed smaller and broader peaks as shown in Fig. S7, indicating that the reconstructed LDH had lower crystallinity as grinding proceeded. Furthermore, as shown in Fig. S8, the SSA of H60-LDH (10.4 $m^2\,g^{-1}$) did not recover as much as before grinding (G0-LDH: 23.8 $m^2\,g^{-1}$), while it became larger than before contacting with H_2O (G60-LDH: 7.9 $m^2\,g^{-1}$). On the other hand, the SSA of G10-LDH (23.9 $m^2\,g^{-1}$) was comparable to that before grinding (G0-LDH: 23.8 $m^2\,g^{-1}$) and did not increase after contact with H_2O (H10-LDH: 23.9 $m^2\,g^{-1}$). These results revealed that

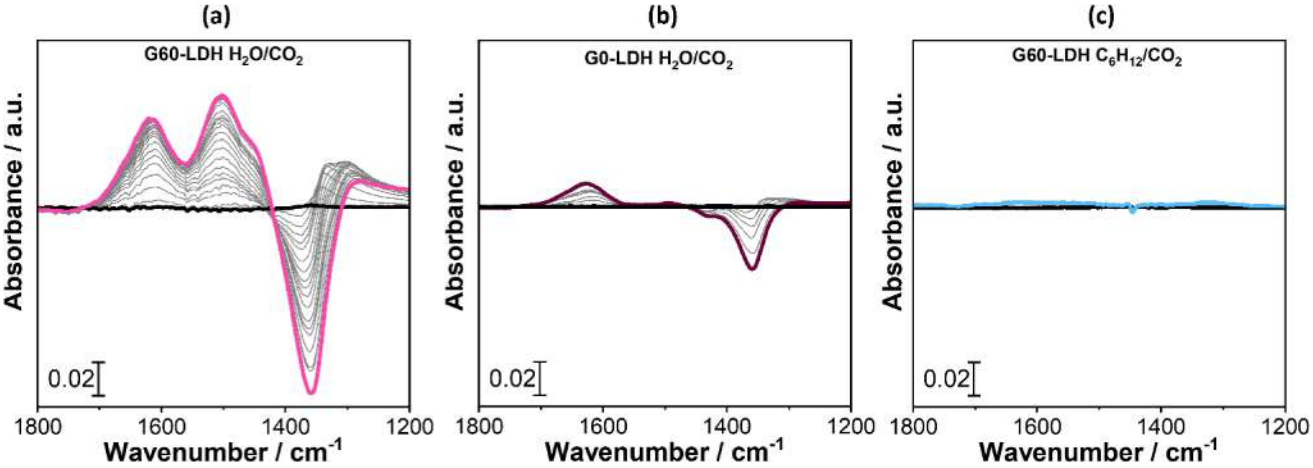

Fig. 4. In-situ ATR-IR spectra in the carbonate-like region (1800–1200 cm^{-1}) of Gx-LDHs [(a) $x = 60$, (b) $x = 0$] under a CO_2-saturated H_2O flow and of (c) G60-LDH under a CO_2-saturated C_6H_{12} flow. The spectra are reported by subtracting the spectra of the N_2-saturated sample to those of the CO_2-saturated sample. Black and colored curves represent N_2-saturated and CO_2-saturated samples, respectively. The curves of intermediate CO_2 coverage are shown in grey.

the memory effect on amorphized Zn–Al LDH did not make a significant increase in SSA and did not fully recover the structural and morphological properties of the pristine Zn–Al LDH.

Besides the difference of SSA, the reconstructed Zn–Al LDH showed different characteristic vibrational features upon CO_2 adsorption compared to the pristine and amorphized Zn–Al LDH. Figs. S9 and S10 show in-situ ATR-IR spectra of G60-LDH obtained by adding N_2- and CO_2-saturated H_2O on the dry samples. Firstly, the evolution of the G60-LDH bands upon contact with N_2-saturated H_2O was observed as shown in Fig. S9. Initially, the G60-LDH sample exhibits two broad bands centered at 1480 and 1410 cm^{-1}. The presence of these two bands differs from what is typically observed in pristine Zn–Al LDH, which is characterized by an intense band at around 1360 cm^{-1}, corresponding to the asymmetric stretching (ν_3) mode of the structural interlayer CO_3^{2-}.[44,45] The appearance of these two bands may be attributed to vibrational modes of intercalated carbonate ions whose coordination environment has been altered by the grinding process. Similar bands have been reported upon heating a Zn–Al LDH, suggesting that structural changes can lead to comparable spectral features.[56] When the G60-LDH is exposed to the N_2-saturated H_2O flow the two bands slowly decreases and the 1360 cm^{-1} signal of the interlayer CO_3^{2-} increases. This behavior is consistent with the memory effect, indicating the transformation from G60-LDH to H60-LDH. Next, after the reconstruction of the LDH structure, the gas was switched to CO_2, and the spectral changes were monitored as shown in Fig. S10. However, as pointed out in some previous works to be able to visualize these spectral changes, the spectra of the N_2-saturated sample should be subtracted to those of the CO_2-saturated sample.[44,45] As spectra obtained by the subtraction, **Fig. 4**(a) corresponds to Fig. S10. Interestingly, a significant increase in intensity of bands in the 1600–1400 cm^{-1} spectral region was observed in Fig. 4(a). In particular, two intense positive bands appear at 1615 and 1500 cm^{-1}, with the latter displaying an additional shoulder at lower wavenumbers. Additionally, a negative band centered at 1360 cm^{-1} and a positive signal in between 1347 and 1200 cm^{-1} arose. Although a complete identification of the bands requires more extensive analysis, insights can still be gained by comparing these results with those previously obtained for G0-LDH and here reported for comparison [Fig. 4(b)]. Notably, G60-LDH exhibits several signals between 1555 and 1425 cm^{-1}, which were almost absent in G0-LDH. Based on previous assignments, these bands may be associated with monodentate carbonate species, which have previously been observed to appear more predominantly in high-performing samples for CO_2RR.[45]

As additional validations for the specific interaction of the reconstructed Zn–Al LDH with CO_2, a further experiment was performed using cyclohexene (C_6H_{12}) instead of H_2O. Notably, the use of C_6H_{12} enables the investigation of N_2 and CO_2 interactions with G60-LDH in its non-reconstructed form, as evidenced by the absence of the 1360 cm^{-1} band upon exposure to an N_2-saturated flow (see blue line in Fig. S11). Following the same procedure used for H_2O, the gas is then switched to CO_2, and the spectra of the N_2-saturated sample were subtracted to the CO_2-saturated sample in order to visualize changes in the spectra. As spectra obtained by the subtraction, Fig. 4(c) corresponds to Fig. S11 and showed no changes in the 1800–1200 cm^{-1} spectral range, suggesting an absence of carbonate formation and low activity of the G60-LDH sample in absence of contact with H_2O (i.e. not reconstructed). To confirm this, the same sample was subsequently exposed to H_2O to enable rehydration. The resulting sample defined as H-G60-LDH was then brought into contact with CO_2-saturated C_6H_{12}, which led to the formation of several bands in the 1800–1200 cm^{-1} region [see Fig. S12(b)].

The ATR results suggest that the G60-LDH exhibits the appearance of some carbonate bands, which are probably monodentate, when in contact with H_2O. These bands could play a role in the reduction of CO_2 to CO under electrolysis conditions.

3.3 CO_2 electrolysis with the as-prepared and ground Zn–Al LDHs

The CO_2RR activity of G*x*-LDHs was evaluated in a three-compartment cell using a three-electrode setup[44] and a 1.0 M $KHCO_3$ aqueous solution as an electrolyte in a potential range from −1.0 to −1.8 V vs. RHE. Gaseous products were detected and quantified by gas chromatography techniques. Only H_2 was detected as a gaseous product under N_2 flow, whereas CO and H_2 were detected as gaseous products under CO_2 flow, indicating that CO_2 originally present within the LDHs does not act as a major substrate for CO_2RR. Regarding the CO_2RR activity of G*x*-LDHs under CO_2 flow, the applied potential dependence of current density (j) and Faradaic efficiency (FE) was shown in Figs. S15 and S16, respectively. Interestingly, G0-LDH (as-prepared LDH) generated H_2 as the major product, while the other G*x*-LDHs (ground LDHs) generated CO as the major product. In both cases, the shortages relative to the total current can be derived from liquid products. We have reported that formic acid was detected as a minor product by CO_2RR with Zn–Al LDH as an electrocatalyst.[44)]

Figure 5 shows the applied potential dependence of j and FE for CO (j_{CO} and FE_{CO}, respectively). As shown in Fig. 5(a), the j_{CO} increased monotonically for all applied potentials and became higher as grinding proceeded. For example, the $|j_{CO}|$ at −1.8 V vs. RHE was 4.4, 14.2, 17.1, 20.7, and 23.0 mA cm^{-2} for $x = 0$, 10, 20, 30, and 60, respectively. Additionally, the FE_{CO} also tends to increase as grinding proceeded as shown in Fig. 5(b), with values of 11–13, 49–51, 47–55, 52–60 and 66–74 % for $x = 0$, 10, 20, 30 and 60, respectively. Since no significant increase in SSA was observed for Zn–Al LDH due to grinding and subsequent reconstruction by contact with H_2O, the increases in the $|j_{CO}|$ and FE_{CO} were not simply due to the exposure effect of latent Zn sites but could be due to the functions of amorphized Zn–Al LDH. Notably, the growth rate in $|j_{CO}|$ was 3.2-fold and 1.6-fold from G0- to G10-LDH and from G10- to G60-LDH, respectively. The relatively large increase in $|j_{CO}|$ from G0- to G10-LDH could be derived from the formation of an amorphous phase at the early stages of grinding as observed by TEM, indicating that it formed preferentially near the particle surface, which is the main catalytic reaction field. The relatively small increase in $|j_{CO}|$ from G10-LDH to G60-LDH is contributed by the transformation of the remaining crystalline phase of Zn–Al LDH into an amorphous phase, indicated by the significant changes in HRTEM images and XAFS spectra from G10- to G60-LDH.

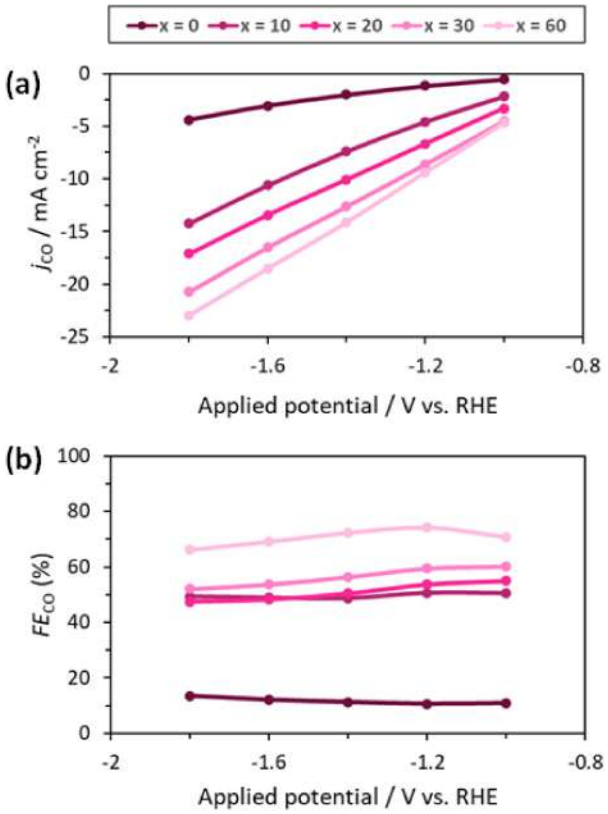

Fig. 5. CO_2RR activity of G*x*-LDHs ($x = 0$, 10, 20, 30, and 60): applied potential dependence of (a) partial current density (j_{CO}) and (b) Faradaic efficiency (FE_{CO}) for CO.

Finally, the effect of electrolysis on the coordination environment and valence state of Zn was evaluated by XAFS analysis. As shown in Fig. S17, G60-LDH after electrolysis at −1.4 V vs. RHE for 10 min showed the XANES spectrum with a more sharpened peak top and shoulder peaks than those before electrolysis, whose shape was similar to that of $ZnCO_3$, although shifted toward the lower energy side. This result indicates that the amorphous phase is retained, and its $Zn^{\delta+}$ state does not change to Zn^0 or Zn^{2+} states after electrolysis. On the other hand, a unique peak at 3.0 Å appeared in the FT-EXAFS spectrum of G60-LDH after electrolysis, which was attributed to Zn–O–M (M: Zn or Al) bonds but was different from that of G*x*-LDHs or Zn compounds, implying that a partial reconstruction of LDH structure progressed under the electrolytic conditions. Since the reconstructed LDH was indicated to have a favorable CO_2 adsorption property for CO_2RR as exhibited by in-situ ATR-IR results, it could also contribute to the enhancement of CO_2RR activity.

4. Conclusions

We prepared Zn–Al LDH and its ground samples (G*x*-LDHs) using simple co-precipitation and grinding methods with a mortar and pestle. XRD and TEM analysis revealed that the collapse of the crystal structure of Zn–Al LDH due to amorphization became more pronounced as grinding proceeded. XAFS analysis indicated that Zn sites in the amorphous phase are mainly in the low-valent Zn state ($Zn^{\delta+}$, $0 < \delta < 2$), which is a favorable state for CO_2-to-CO conversion. Evidently, G*x*-LDHs exhibited superior activity for CO_2-to-CO conversion as grinding proceeded. G60-LDH generated CO with a faradaic efficiency of 74 % at −1.2 V vs. RHE and with a partial current density of 23.0 mA cm^{-2} at −1.8 V vs. RHE. ATR results evidenced for G60-LDH the appearance, upon contact with a CO_2-saturated H_2O, of some bands due to monodentate carbonates, whose role was identified as crucial in the reduction of CO_2 to CO under electrolysis conditions. All these results highlight the crucial effect of grinding treatment of Zn–Al LDH on its CO_2RR activity. This finding will help us understand the importance of grinding treatment for fragile catalysts such as LDH, identify their true active species, and discover superior catalysts in the field of CO_2 electrolysis.

Acknowledgement This research was supported through 4AirCRAFT project under the strategic international cooperation between Europe (Horizon2020, No. 101022633) and Japan Science and Technology Agency (JST, No. JPMJSC2102). 4AirCRAFT project is also supported by The Sao Paulo Research Foundation (FAPESP, No. 2022/04751-0). This work was also supported by Japan Society for the Promotion of Science Grants-in-Aid for Scientific Research (JSPS KAKENHI, No. 24K01152). M.C., V. C. and F.B. acknowledge support from the ProjectCH4.0 under the MUR program “Dipartimenti di Eccellenza 2023–2027” (CUP: D13C22003520001) and the NODES project funded by the European Union NextGenerationEU (Mission 4, Component 1.5, ECS00000036–CUP: D17G2200015000). M.Q. and J.H. acknowledge the Hercules fund ‘Direct electron detector for soft matter TEM’ from Flemish Government for the purchase of the K2 DED. Dr. Melodj Dosa is acknowledged for the ATR measurements in cyclohexene and for fruitful discussion. The XAFS experiments were conducted at the BL5S1 of Aichi Synchrotron Radiation Center, Aichi Science & Technology Foundation, Aichi, Japan (Proposal No. 202204007).

Supporting information Figures and photographs that could not be included in the main part of this paper can be referred to as “Supplemental materials”.

References

1) M. Morimoto, Y. Takatsuji, K. Hirata, T. Fukuma, T. Ohno, T. Sakakura and T. Haruyama, *Electrochim. Acta* 290, 255 (2018).
2) M. Zhao, Y. Gu, P. Chen, Z. Xin, H. Zhu, B. Wang, K. Zhu, S. Yan and Z. Zou, *J. Mater. Chem. A* 7, 9316 (2019).
3) B. Ren, Z. Zhang, G. Wen, X. Zhang, M. Xu, Y. Weng, Y. Nie, H. Dou, Y. Jiang, Y. Deng, G. Sun, D. Luo, L. Shui, X. Wang, M. Feng, A. Yu and Z. Chen, *Adv. Mater.* 34, 1 (2022).
4) A. Tatin, J. Bonin and M. Robert, *ACS Energy Lett.* 1, 1062 (2016).
5) P. De Luna, C. Hahn, D. Higgins, S. A. Jaffer, T. F. Jaramillo and E. H. Sargent, *Science* 364, eaav3506 (2019).
6) J. Qiao, Y. Liu, F. Hong and J. Zhang, *Chem. Soc. Rev.* 43, 631 (2014).
7) C. D. Keeling, S. C. Piper, R. B. Bacastow, M. Wahlen, T. P. Whorf, M. Heimann and H. A. Meijer, in “A History of Atmospheric CO_2 and Its Effects on Plants, Animals, and Ecosystems”, Ed. by I. T. Baldwin, M. M. Caldwell, G. Heldmaier, R. B. Jackson, O. L. Lange, H. A. Mooney, E. D. Schulze, U. Sommer, J. R. Ehleringer, M. Denise Dearing and T. E. Cerling, Springer-Verlag, New York (2001) pp. 83–113.
8) X. Lan, P. P. Tans and K. W. Thoning, “Trends in globally-averaged CO_2 determined from NOAA Global Monitoring Laboratory measurements”. https://gml.noaa.gov/ccgg/trends/global.html (2025).
9) K. Kamiya, K. Fujii, M. Sugiyama and S. Nakanishi, *Chem. Lett.* 50, 166 (2021).
10) J. M. Spurgeon and B. Kumar, *Energ. Environ. Sci.* 11, 1536 (2018).
11) W. Zhu, R. Michalsky, Ö. Metin, H. Lv, S. Guo, C. J. Wright, X. Sun, A. A. Peterson and S. Sun, *J. Am. Chem. Soc.* 135, 16833 (2013).
12) S. Verma, Y. Hamasaki, C. Kim, W. Huang, S. Lu, H.-R. M. Jhong, A. A. Gewirth, T. Fujigaya, N. Nakashima and P. J. A. Kenis, *ACS Energy Lett.* 3, 193 (2018).
13) M. Ma, K. Liu, J. Shen, R. Kas and W. A. Smith, *ACS Energy Lett.* 3, 1301 (2018).
14) X. Zhang, S.-X. Guo, K. A. Gandionco, A. M. Bond and J. Zhang, *Mater. Today Adv.* 7, 100074 (2020).
15) D. L. T. Nguyen, M. S. Jee, D. H. Won, H. Jung, H.-S. Oh, B. K. Min and Y. J. Hwang, *ACS Sustain. Chem. Eng.* 5, 11377 (2017).
16) W. Luo, Q. Zhang, J. Zhang, E. Moioli, K. Zhao and A. Züttel, *Appl. Catal. B-Environ.* 273, 119060 (2020).
17) I. Stamatelos, C. T. Dinh, W. Lehnert and M. Shviro, *ACS Appl. Energ. Mater.* 5, 13928 (2022).
18) Z. Geng, X. Kong, W. Chen, H. Su, Y. Liu, F. Cai, G. Wang and J. Zeng, *Angew. Chem.* 130, 6162 (2018).
19) Z. Ling, Y. Yin, X. Kang, X. Li, R. Duan, S. Zhou, H. Liu, G. Mo, Z. Chen, X. Wu, R. Feng, Z. Wu, B. Han and X. Xing, *Chem. Catal.* 5, 101192 (2025).
20) C. Li, G. Shen, R. Zhang, D. Wu, C. Zou, T. Ling, H. Liu, C. Dong and X.-W. Du, *J. Mater. Chem. A* 7, 1418 (2019).
21) X. Y. Zhang, W. J. Li, J. Chen, X. F. Wu, Y. W. Liu, F. Mao, H. Y. Yuan, M. Zhu, S. Dai, H. F. Wang, P. Hu, C. Sun, P. F. Liu and H. G. Yang, *Angew. Chem. Int. Edit.* 61, e202202298 (2022).
22) Q. Liu, B. He, D. Zheng, X. Zhou, X. Zhang, J. Huang, Y. Wang, W. Lai and Z. Gu, *Small* 20, 1 (2024).
23) S. Li, S. Zhao, X. Lu, M. Ceccato, X. Hu, A. Roldan, J. Catalano, M. Liu, T. Skrydstrup and K. Daasbjerg, *Angew. Chem. Int. Edit.* 60, 22826 (2021).
24) F. Yang, P. Song, X. Liu, B. Mei, W. Xing, Z. Jiang, L. Gu and W. Xu, *Angew. Chem. Int. Edit.* 57, 12303 (2018).
25) J. Chen, Z. Li, X. Wang, X. Sang, S. Zheng, S. Liu, B. Yang, Q. Zhang, L. Lei, L. Dai and Y. Hou, *Angew. Chem. Int. Edit.* 134, e202111683 (2022).
26) S. Wei, J. Zhu, X. Chen, R. Yang, K. Gu, L. Li, C.-Y. Chiang, L. Mai and S. Chen, *Nat. Commun.* 16, 1652 (2025).
27) Y. Wang, S. Luo, Z. Wang and Y. Fu, *Appl. Clay Sci.* 80–81, 334 (2013).
28) Y. Arishige, D. Kubo, K. Tadanaga, A. Hayashi and M. Tatsumisago, *Solid State Ionics* 262, 238 (2014).

29) L. Lu, Y. Zheng, R. Yang, A. Kakimov and X. Li, *Mater. Today Chem.* 21, 100488 (2021).

30) H. Koshikawa, H. Murase, T. Hayashi, K. Nakajima, H. Mashiko, S. Shiraishi and Y. Tsuji, *ACS Catal.* 10, 1886 (2020).

31) M. Sreenivasulu, A. Hadrihalli, M. A. Alshehri and N. P. Shetti, *Energ. Fuel.* 38, 12888 (2024).

32) Y. Iwai, A. Miura, N. C. Rosero-Navarro, M. Higuchi and K. Tadanaga, *J. Asian Ceram. Soc.* 7, 147 (2019).

33) H. Kowsari, M. Mehrpooya and F. Pourfayaz, *Int. J. Hydrogen Energ.* 45, 27129 (2020).

34) Z. Yuan, S. M. Bak, P. Li, Y. Jia, L. Zheng, Y. Zhou, L. Bai, E. Hu, X. Q. Yang, Z. Cai, Y. Sun and X. Sun, *ACS Energy Lett.* 4, 1412 (2019).

35) C. I. Ezeh, M. Tomatis, X. Yang, J. He and C. Sun, *Ultrason. Sonochem.* 40, 341 (2018).

36) K. Tadanaga, Y. Furukawa, A. Hayashi and M. Tatsumisago, *Adv. Mater.* 22, 4401 (2010).

37) D. Kubo, K. Igarashi, S. Ishiyama, N. C. Rosero Navarro, A. Miura, M. Higuchi and K. Tadanaga, *J. Ceram. Soc. Jpn.* 127, 788 (2019).

38) G. Miao, L. Liu, X. An and X. Wu, *Chinese J. Chem. Eng.* 64, 156 (2023).

39) K. Iwase, T. Hirano and I. Honma, *ChemSusChem* 15, e202102340 (2022).

40) M. Serafini, F. Mariani, A. Fasolini, E. T. Brandi, E. Scavetta, F. Basile and D. Tonelli, *Adv. Funct. Mater.* 33, 1 (2023).

41) F. Tan, T. Liu, E. Liu and Y. Zhang, *Catal. Lett.* 154, 11 (2024).

42) X. Ma, T. Liu, B. Lu and Y. Zhang, *J. Alloy. Compd.* 973, 172858 (2024).

43) N. Yamaguchi, R. Nakazato, K. Matsumoto, M. Kakesu, N. C. Rosero-Navarro, A. Miura and K. Tadanaga, *J. Asian Ceram. Soc.* 11, 406 (2023).

44) R. Nakazato, K. Matsumoto, N. Yamaguchi, M. Cavallo, V. Crocellà, F. Bonino, M. Quintelier, J. Hadermann, N. C. Rosero-Navarro, A. Miura and K. Tadanaga, *Electrochemistry* 91, 23 (2023).

45) M. Cavallo, M. Dosa, R. Nakazato, N. G. Porcaro, M. Signorile, M. Quintelier, J. Hadermann, S. Bordiga, N. C. Rosero-Navarro, K. Tadanaga, V. Crocellà and F. Bonino, *J. CO_2 Util.* 83, 102804 (2024).

46) R. Nakazato, K. Matsumoto, M. Quintelier, J. Hadermann, N. C. Rosero-Navarro, A. Miura and K. Tadanaga, *Open Ceram.* 22, 100788 (2025).

47) F. Loprete, E. Tosi Brandi, F. Calcagno, J. De Maron, A. Fasolini, R. Tarroni, F. Basile and I. Rivalta, *Chem. Rec.* 25, e202500014 (2025).

48) M. Yasaei, M. Khakbiz, A. Zamanian and E. Ghasemi, *Mat. Sci. Eng. C-Mater.* 103, 109816 (2019).

49) Y. Zhao, G. Chen, T. Bian, C. Zhou, G. I. N. Waterhouse, L. Z. Wu, C. H. Tung, L. J. Smith, D. O'Hare and T. Zhang, *Adv. Mater.* 27, 7824 (2015).

50) S. Guo, Y. Du, H. Luo, Z. Zhu, T. Ouyang and Z. Liu, *Angew. Chem. Int. Edit.* 63, e202314099 (2024).

51) G. Chen, Y. Zhao, L. Shang, G. I. N. Waterhouse, X. Kang, L. Wu, C. Tung and T. Zhang, *Adv. Sci.* 3, 1500424 (2016).

52) J. Wang, Z. Zhu, Y. Lin, Z. Li, W. Tang, J. Wang, J. S. Chen and R. Wu, *Carbon Neutralizat.* 3, 423 (2024).

53) E. S. Jeong, H. J. Yu, Y. J. Kim, G. C. Yi, Y. D. Choi and S. W. Han, *J. Nanosci. Nanotechno.* 10, 3562 (2010).

54) S. Xu, J. Zhao, Q. Yu, X. Qiu and K. Sasaki, *ACS Earth Space Chem.* 3, 2175 (2019).

55) P. Koilraj and K. Srinivasan, *Ind. Eng. Chem. Res.* 50, 6943 (2011).

56) K. Matsuda, A. Okuda, N. Iio, N. Tarutani, K. Katagiri and K. Inumaru, *Inorg. Chem.* 63, 15634 (2024).